

# Rapid tremor migration during few minute-long slow earthquakes in Cascadia

B. Gombert<sup>a,\*\*</sup>, J. C. Hawthorne<sup>a,\*</sup>

<sup>a</sup>*Department of Earth Sciences, University of Oxford, U.K.*

---

## Abstract

Slow earthquakes are now commonly found to display a wide range of durations, moments, and slip and propagation speeds. But not all types of slow earthquakes have been examined in detail. Here we probe tremor bursts with durations between 1 and 30 minutes, which are likely driven by few minute-long bursts of aseismic slip. We use a coherence-based technique to detect thousands of tremor bursts beneath Vancouver Island in Cascadia. Then we examine 17 of the ruptures by tracking their evolving tremor locations over an 8-km region. We find that tremor migrates at rates of 2 to 30 m/s and that shorter bursts migrate faster. The rapid propagation of the shorter bursts provides a new observation, which must be reproduced by a complete model of slow earthquakes. And though some observational biases persist, the short events' speeds appear to fill a gap in the spectrum of observed slow earthquakes. They may provide further evidence that whatever fault zone process creates slow earthquakes, it must allow for faster slip and propagation in smaller ruptures.

*Keywords:* tremor, earthquake, slow slip, Cascadia, seismology

---

1 Identify rapid propagation of tremor in 1 to 30 minute-long tremor bursts

---

\*Corresponding author

\*\*Now at Collecte Localisation Satellite, Toulouse, France

*Email address:* [jessica.hawthorne@earth.ox.ac.uk](mailto:jessica.hawthorne@earth.ox.ac.uk) (J. C. Hawthorne)

2 Among observed bursts, shorter events propagate faster  
3 Propagation fills in an observational gap along the slow earthquake spectrum  
4 May suggest that a single mechanism creates ruptures with wide-ranging slip rates  
5 But other observational gaps in the slow earthquake spectrum remain

## 6 **1. Introduction**

7 We now frequently observe slow earthquakes with a wide range of sizes and slip rates.  
8 However, some types of slow earthquakes are recorded more often and in more detail than  
9 others. The largest slow earthquakes, known as slow slip events (SSEs), are well observed.  
10 They typically last weeks to months and can rupture several hundred km-long portions of  
11 the plate interface at subduction zones (e.g., Dragert et al., 2001; Kostoglodov et al., 2003;  
12 Obara et al., 2004; Douglas et al., 2005; Vaca et al., 2018). The slipping location in slow slip  
13 events often migrates along strike at rates of 5 to 10 km per day, and the slip rate at each  
14 location is of order  $10^{-7}$  m/s, around 100 times faster than the plate convergence rate (e.g.,  
15 Miller et al., 2002; Obara and Sekine, 2009; Wech et al., 2009; Bartlow et al., 2011).

16 However, slow slip events are not simple, smoothly migrating ruptures. They often  
17 contain subevents: bursts of more rapid slip. In Cascadia, the longest identified subevents  
18 are several day-long intervals with more rapid slip or migration (e.g., Kao et al., 2006;  
19 Wech and Bartlow, 2014). Few hour-long subevents are also well recognised; they create  
20 rapid tremor reversals (RTRs) in Cascadia and Japan. During RTRs, tremor migrates  
21 to 50 km backward along strike, through regions that have already slipped in the main  
22 event's forward migration. This reversed migration is rapid: 10 to 40 times faster than

23 main event’s forward migration (Obara, 2010; Houston et al., 2011; Yamashita et al., 2015;  
24 Thomas et al., 2013; Royer et al., 2015; Bletery et al., 2017). Geodetic data reveal that the  
25 tremor migration coincides with and is likely driven by few hour-long bursts of accelerated  
26 aseismic slip. Slip rates are around  $10^{-6}$  m/s, an order of magnitude faster than the main  
27 event slip rate (Hawthorne et al., 2016).

28 Slightly shorter subevents, with durations between a few minutes and a few hours, have  
29 not yet been observed geodetically but are frequently suggested by varying tremor migration  
30 and amplitude. In Cascadia, tremor often migrates 40 to 60 km along dip during hour-long  
31 tremor streaks, moving 50 to 500 times faster than the main front (Ghosh et al., 2010). And  
32 tremor migrates up to 20 km in a range of directions during 10 to 30-minute-long rapid  
33 tremor migrations (RTMs), moving 10 to 50 times faster than the main front (Rubin and  
34 Armbruster, 2013; Peng et al., 2015; Peng and Rubin, 2016; Bletery et al., 2017). Similar  
35 10- to 50-km-long tremor migration has also been observed in Japan, Taiwan, California,  
36 Mexico, and Alaska (e.g., Ide, 2010b; Shelly, 2010; Obara, 2012; Sun et al., 2015; Peng and  
37 Rubin, 2017). Migration rates vary among these locations, but shorter events are usually  
38 found to propagate faster.

39 Tremor migration has not yet been observed in detail on timescales shorter than 10  
40 minutes, but several features of tremor suggest that complex, rapid propagation should  
41 continue to short timescales. First, tremor varies in amplitude on a range of timescales, from  
42 seconds to days (Obara, 2002; Shelly et al., 2006; Ghosh et al., 2010; Ide, 2010a), and those  
43 variations are correlated with aseismic deformation (Hawthorne and Rubin, 2013b; Frank,

44 2016). Second, some 20 to 200 second-long increases in tremor amplitude are associated with  
45 20 to 200 second-long increases in slow slip moment rate. These moment rate increases are  
46 observable in long-period seismic data, and the 20 to 50 second-long events are called very  
47 low frequency earthquakes, or VLFs (e.g., Ito and Obara, 2006; Takeo et al., 2010; Walter  
48 et al., 2013; Hutchison and Ghosh, 2016; Maury et al., 2016; Baba et al., 2020).

49 In this study, we identify and analyse tremor bursts with durations between 1 and 30 min-  
50 utes. Many of these events are slightly longer than VLFs but shorter than previously  
51 detected (>10-minute) tremor migrations. We first identify thousands of tremor bursts in  
52 Cascadia and then analyse 17 of them in more detail. We identify rapid tremor migration  
53 which likely reflects rapid migration of aseismic slip.

## 54 **2. Motivation to Constrain the Spectrum of Subevents**

55 We analyse migration on few-minute timescales for two reasons: (1) because we wish to  
56 more fully observe the range of behaviours in slow earthquakes and (2) because the range  
57 of slip speeds and behaviours could help us determine which fault zone process creates slow  
58 earthquakes. The propagation speeds of few hour-long subevents have already been used to  
59 test some models of slow earthquakes (Ariyoshi et al., 2009; Rubin, 2011; Luo and Ampuero,  
60 2017; Luo and Liu, 2021). Some researchers have proposed that rapid subevents could reflect  
61 the rupture of asperities or asperity clusters embedded in the slow slip region. They have  
62 successfully produced the propagation speeds of few hour-subevents (RTRs) propagation  
63 speeds with a relatively simple approach: by mixing unstable patches into a region with a  
64 nominally stable slow slip rheology. The unstable patches effectively increase the local stress

65 drop and drive more rapid slip (Ariyoshi et al., 2009; Colella et al., 2012; Peng and Rubin,  
 66 2018; Luo and Liu, 2021).

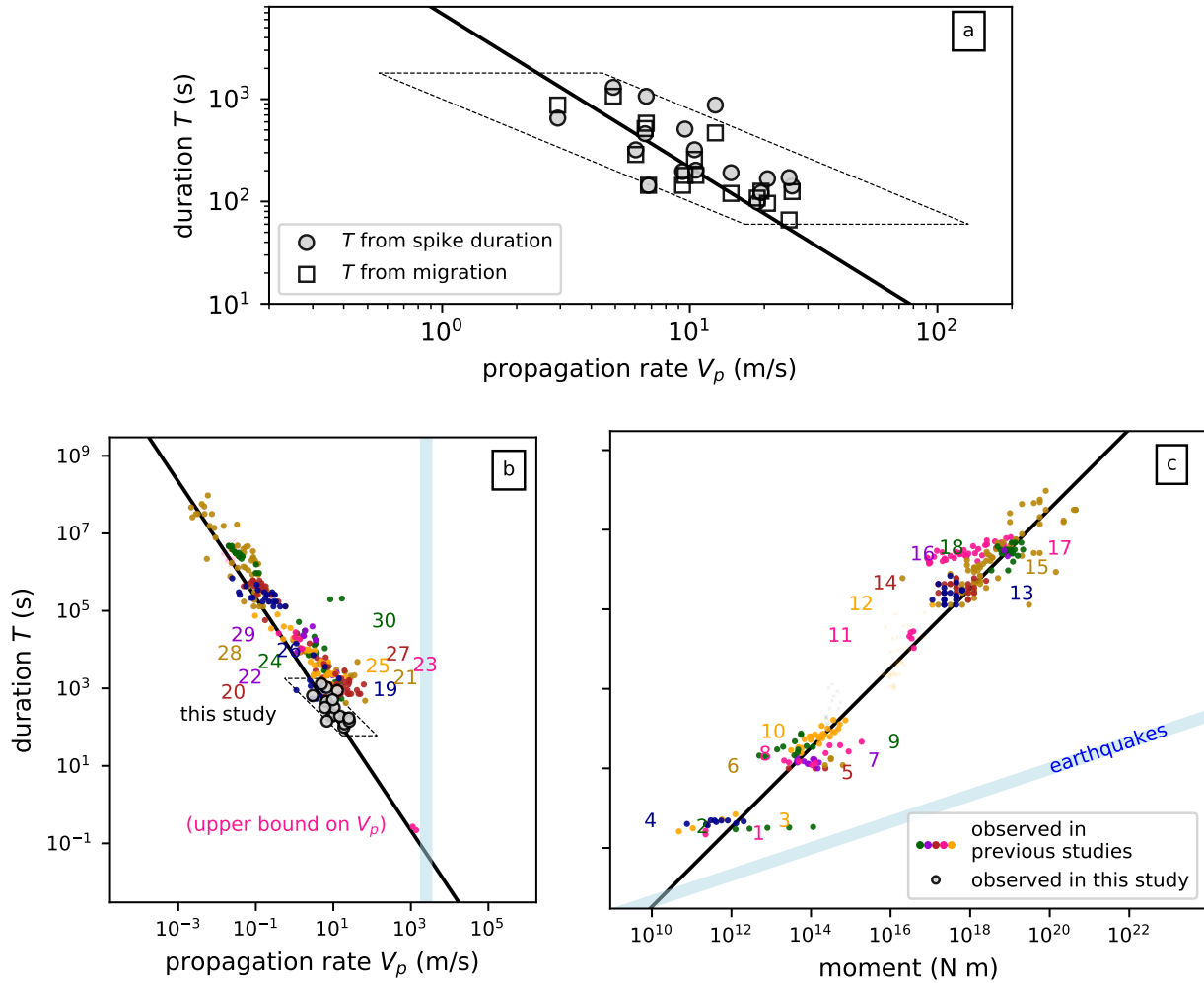


Figure 1: Caption on next page.

67 However, it may not be plausible that slip speed increases by many orders of magnitude  
 68 simply because the stress drop that drives rupture increases. For many of the proposed slow  
 69 slip rheologies, the stress drop required for rupture increases dramatically as the rupture  
 70 speed increases (Hawthorne and Rubin, 2013c). It may be that increased local stress drops  
 71 can provide enough energy to increase the rupture speed by a factor of 10 to 20, as seen in

Figure 1: **a)** Duration versus propagation velocity for tremor bursts examined in this study. Filled circles indicate durations obtained from the widths of peaks in the  $C_p^{com}$  records while open squares indicate the durations of observable migration. The dashed parallelogram bounds the types of events we can observe with our approach. The solid black lines in panels a-c indicate a propagation rate that scales as  $T^{-1/2}$  and a moment equal to  $3 \times 10^{12}$  N-m times  $T$ . We map the line from panel c to the panels a and b assuming a rectangular rupture with a 3:1 aspect ratio and a 30-kPa stress drop. **b)** Duration vs propagation velocity and **c)** duration vs moment for our observations as well as for a selection of previous studies, indexed by the numbers below. Note that trends are visible in some studies but that there is often more uncertainty when comparing between locations. Further, to avoid clutter, we plot only a handful of observations randomly selected from each study when a large number of events are detected. Further, many authors publish only a single average propagation rate and uncertainty, or they plot a handful of figures. In those cases, we choose one or a few number from the published distribution or extract rough propagation rates from the figures. Values are taken from 1: Shelly (2017); Thomas et al. (2016); Hawthorne et al. (2019), 2: Farge et al. (2020), 3: Supino et al. (2020), 4: Bostock et al. (2015), 5: Ito et al. (2007), 6: Matsuzawa et al. (2009), 7: Maury et al. (2016), 8: Yabe et al. (2021), 9: Takeo et al. (2010), 10: Ide et al. (2008), 11: Royer et al. (2015); Hawthorne et al. (2016), 12: Itaba and Ando (2011), 13: Kitagawa et al. (2011); Itaba et al. (2013); Ochi et al. (2016), 14: Sekine et al. (2010), 15: Gao et al. (2012), 16: Rousset et al. (2017), 17: Michel et al. (2019), 18: Tu and Heki (2017), 19: Rubin and Armbruster (2013), 20: Ghosh et al. (2010), 21: Sun et al. (2015), 22: Cruz-Atienza et al. (2018), 23: Shelly (2010), 24: Peng and Rubin (2016), 25: Bletery et al. (2017), 26: Obara (2012), 27: Peng and Rubin (2017), 28: Peng et al. (2015), 29: Houston et al. (2011), and 30: Yamashita et al. (2015).

72 RTRs, but a factor of 100 or 1000 rupture speed increases may require a spatial variation in  
73 the *resistance* to accelerating slip.

74 Such spatially variable resistance to slip is intriguing because it should not exist for  
75 several of the proposed slow slip rheologies. For instance, if slow slip events happen because

76 the rheology at depth imposes a temperature-dependent speed limit (e.g., Shibazaki and  
77 Iio, 2003; Shibazaki and Shimamoto, 2007; Hawthorne and Rubin, 2013a), that speed limit  
78 should stay roughly the same throughout the slow slip region, where the temperature stays  
79 relatively uniform.

80 There is, of course, already evidence that slow earthquake slip rates vary by at least four  
81 orders of magnitude, from  $10^{-7}$  m/s in slow slip to 0.1 or 1 mm/s in VLFES and tremor  
82 (e.g., Dragert et al., 2001; Bartlow et al., 2011; Bostock et al., 2015). However, it remains  
83 controversial whether tremor, VLFES, and tremor bursts, are created by the same rheology  
84 that governs slow slip slip rates. A single fault zone rheology is suggested by a systematic  
85 trend in *observed* slow earthquakes: smaller events are faster. In Figure 1b, we plot the  
86 propagation speeds and durations of tremor bursts from a variety of studies, and we see that  
87 shorter tremor bursts migrate faster. In Figure 1c, we plot the moments and durations of  
88 slow earthquakes from a variety of studies, as was done by Ide et al. (2007), and we see that  
89 observed slow earthquakes' moments  $M_0$  scale roughly linearly with their duration  $T$ . Note  
90 that if we assume that slow earthquakes have magnitude-independent stress drops, as weakly  
91 suggested by observations of slow slip events, RTRs, and LFEs (Gao et al., 2012; Hawthorne  
92 et al., 2016; Chestler and Creager, 2017), a linear moment-duration scaling implies that slip  
93 rate scales as  $M_0^{-1/2}$ . Since the linear moment-duration trend appears to extend all the way  
94 from  $M_w$  7 slow slip events to  $M_w$  1 LFEs, it would seem sensible to start assessing which  
95 rheologies would allow slip speeds that are  $10^4$  times faster on 400-m LFE patches than on  
96 400-km slow slip regions.

97 At this point, however, it is also sensible to recall that the scalings between moment, du-  
98 ration, and slip rate remain uncertain. Other moment-duration scaling have been observed.  
99 Bostock et al. (2015) and Farge et al. (2020) inferred a very weak moment-duration scaling,  
100 with  $T \sim M_0^0$  or  $M_0^{0.1}$ , among the low frequency earthquakes that compose tremor. Michel  
101 et al. (2019) and Supino et al. (2020) identified a moment-duration scaling similar to that  
102 seen in normal earthquakes, with  $T \sim M_0^{1/3}$  among geodetically observed slow slip events and  
103 among sub-second tremor bursts, respectively. Further, the linear moment-duration trend  
104 identified by Ide et al. (2007) depends on connecting days to months-long slow slip events  
105 and seconds-long LFEs and VLFES (Figure 1c). And there are significant gaps along that  
106 trend. We now have abundant observations of sub-second LFEs, 10-second VLFES, and days  
107 to months-long slow slip events, but there are fewer observations between those durations,  
108 and there may be missing observations that fall off the trend (Gomberg et al., 2016).

109 To overcome all the observational gaps, we will require a wide range of approaches. For  
110 instance, recent work has suggested an expansion of the tremor band to longer durations  
111 (Kaneko et al., 2018; Masuda et al., 2020). Here we focus on a different band and attempt to  
112 expand the range of slow slip subevents to shorter durations: between 2 and 10 minutes. We  
113 modify our tremor detection methodology to search for the expected short, rapid migration  
114 on these timescales, and we partly fill the apparent gap in the duration-propagation rate  
115 trend (Figure 1b). We note, however, that our approach still suffers from observational bias;  
116 it was not designed to find events that are much faster or slower than the along-trend speeds.

117 In the sections that follow, we first describe our phase coherence-based tremor detection



118 approach (section 3) and the available data and processing (section 4). Then we describe  
 119 the observed large-scale tremor migration patterns in section 5, examine small-scale tremor  
 120 migration in 17 tremor bursts in section 6, and discuss the migrations' implications in sec-  
 121 tion 7.

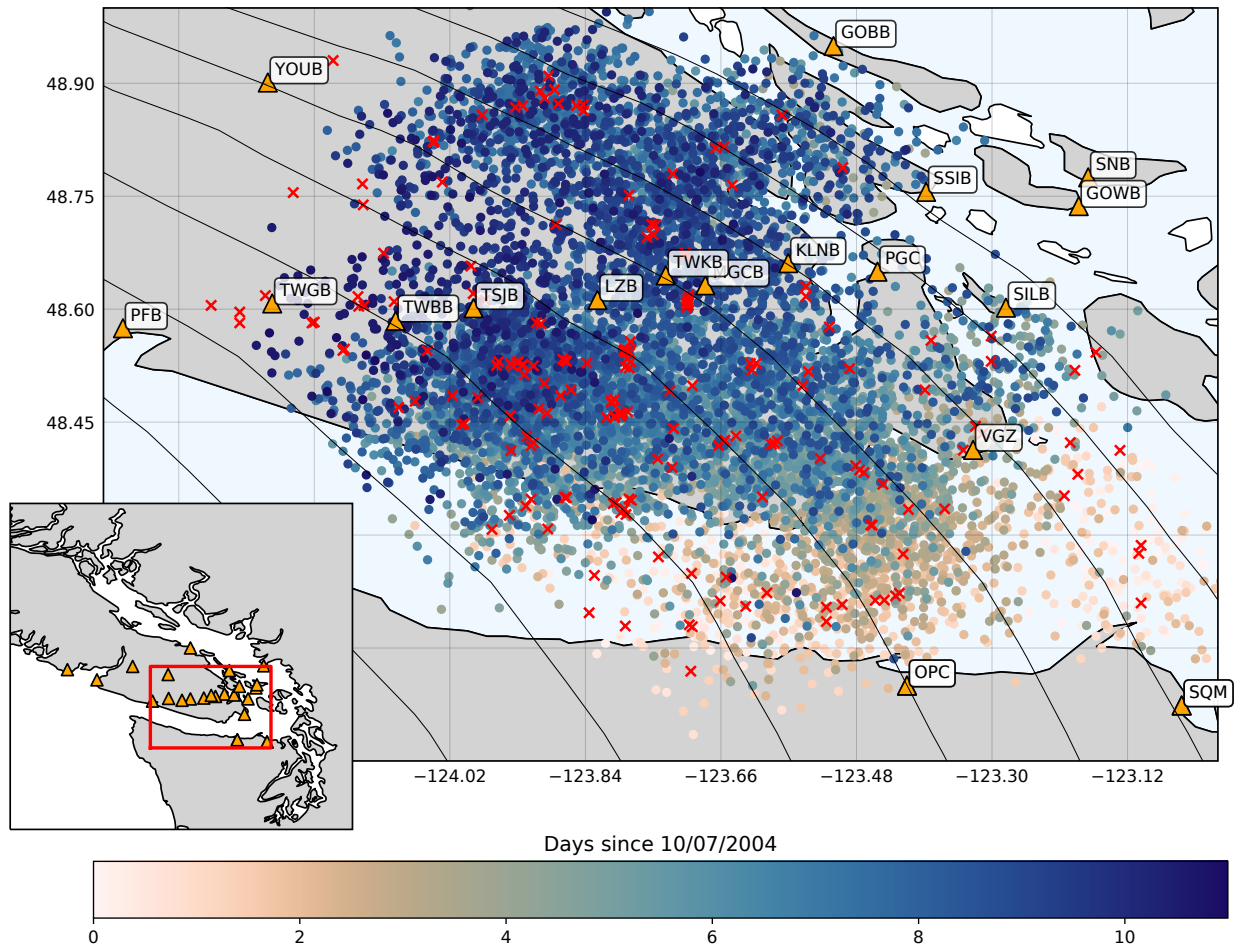


Figure 2: **Map of study area.** Orange triangles are the seismic stations used in 2004. Red crosses are the 130 LFEs locations from (Bostock et al., 2012). Circles mark spikes in inter-component coherence, coloured by time. They are plotted at random locations within 5 km of the template LFE used in the coherence calculation. Black lines are the 30 to 44-km depth contours from McCrory et al. (2012), spaced every 2 km.

### 122 3. Tremor Detection Method: Identifying Tremor Near Template Locations

123 To identify and locate tremor, we use a phase coherence-based approach developed by  
124 Hawthorne and Ampuero (2017), which is a variant of empirical matched field techniques  
125 (e.g., Bucker, 1976; Harris and Kvaerna, 2010; Corciulo et al., 2012; Wang et al., 2015).  
126 This approach allows us to identify tremor that ruptures fault patches close to known low  
127 frequency earthquakes (LFEs). The coherence calculation is able to identify tremor even if  
128 the tremor ruptures are complex or if the tremor consists of a series of ruptures, as the method  
129 combines two common approaches to identifying tremor. First, as inspired by matched filter  
130 techniques (Brown et al., 2008; Bostock et al., 2012; Frank et al., 2014; Shelly, 2017), the  
131 calculation compares seismograms between events. It assesses whether the template and  
132 target signals could have the same Green’s functions: if they result from the same source-  
133 station path. Second, as inspired by cross-station techniques (Armbruster et al., 2014; Peng  
134 et al., 2015; Savard and Bostock, 2015), the calculation compares seismograms between  
135 stations or components. It assesses whether the signals at all stations or components could  
136 result from the same tremor source time functions.

#### 137 3.1. Inter-Station Coherence

138 In all of the coherence calculations, we begin with a set of template seismograms  $d_{tkm}$   
139 that were created by Bostock et al. (2012) and which represent the signals generated by  
140 LFEs occurring at 130 locations on the plate interface (red crosses in Figure 2). The LFEs  
141 are recorded at a range of stations  $k$  and on three components  $m$  (east, north, and up).  
142 We compare the template seismograms at each station with 30 to 60-second-long intervals

143 of target seismic data ( $d_{dkm}$ ). To assess whether a 30 or 60-second interval contains tremor  
 144 coming from the same location as the template, we compute the inter-station phase coherence  
 145 at a range of frequencies  $f$ :

$$C_p^{sta}(f) = \frac{1}{3} \sum_{m=1}^3 \frac{2}{N(N-1)} \sum_{k=1}^N \sum_{l=k+1}^N \operatorname{Re} \left[ \frac{\hat{d}_{dkm} \hat{d}_{tkm}^* \hat{d}_{dlm}^* \hat{d}_{tllm}}{|\hat{d}_{dkm} \hat{d}_{tkm} \hat{d}_{dlm} \hat{d}_{tllm}|} \right]. \quad (1)$$

146 Here  $\hat{d}_{tkm}(f)$  and  $\hat{d}_{dkm}(f)$  are the Fourier transforms of the template and target data at  
 147 station  $k$  and component  $m$ , and we compare between stations  $k$  and  $l$  in each term. There  
 148 are  $N$  stations in total, and we average over the  $N(N-1)/2$  station pairs and over the three  
 149 components at each station. Note that we have dropped the frequency indexing on the right  
 150 hand side for readability, and we also average over frequencies  $f$  between 1 and 6 Hz.

151 Note that if the target seismograms  $d_{dkm}$  record tremor from the same location as the  
 152 template seismograms, then the template and target seismograms may be written as  $\hat{d}_{tkm} =$   
 153  $\hat{s}_t \hat{g}_{km}$  and  $\hat{d}_{dkm} = \hat{s}_d \hat{g}_{km}$ , where  $\hat{s}_t$  and  $\hat{s}_d$  are the template and target tremor source time  
 154 functions,  $\hat{g}_{km}$  is the path effect, and  $C_p^{sta}$  becomes

$$C_p^{sta}(f) = \frac{1}{3} \sum_{m=1}^3 \frac{2}{N(N-1)} \sum_{k=1}^N \sum_{l=k+1}^N \operatorname{Re} \left[ \frac{(\hat{s}_t \hat{g}_{km})(\hat{s}_d^* \hat{g}_{km}^*)(\hat{s}_t^* \hat{g}_{lm}^*)(\hat{s}_d \hat{g}_{lm})}{|\hat{s}_t \hat{s}_d \hat{g}_{km} \hat{g}_{lm}|^2} \right] = 1. \quad (2)$$

155 So by identifying intervals with high phase coherence  $C_p^{sta}$ , near 1, we can identify intervals  
 156 when tremor is occurring at the same location as previously located templates. Synthetic  
 157 tests suggest that  $C_p^{sta}$  is significantly larger than zero only when tremor occurs within about  
 158 0.5 km from the template: within a fraction of one seismic wavelength (Figure S3).

### 159 3.2. Inter-Component Coherence

160 In some cases, however, we do not need or want 0.5-km precision. We simply wish to  
 161 know whether tremor is occurring in *roughly* the same area as the template: within 10 km

162 or so. In such situations, we compute an inter-component phase coherence:

$$C_p^{com}(f) = \frac{1}{N} \sum_{k=1}^N \frac{2}{3(3-1)} \sum_{m=1}^3 \sum_{n=m+1}^3 \operatorname{Re} \left[ \frac{\hat{d}_{dkm} \hat{d}_{tkm}^* \hat{d}_{dkn}^* \hat{d}_{tkn}}{|\hat{d}_{dkm} \hat{d}_{tkm} \hat{d}_{dkn} \hat{d}_{tkn}|} \right]. \quad (3)$$

163 Here we multiply the Fourier domain seismograms across components  $m$  and  $n$  rather than  
 164 across stations  $k$ . Then we average over component pairs and over stations.

165 To understand why  $C_p^{com}$  is often high even when the target tremor is slightly offset from  
 166 the template, note that when the tremor is close to the template, its Green's functions are  
 167 likely to have shapes similar to the template's Green's function. The tremor Green's functions  
 168  $g'_{km}(t)$  may simply be time-shifted versions of the template Green's functions  $g_{km}(t)$ . They  
 169 may be approximated by  $g'_{km} = g_{km}(t - \Delta t)$ , where the time shift  $\Delta t$  results from the  
 170 difference in travel time to the source. Now we may note that if we have multiple recording  
 171 on the same station, just at different components  $m$  and  $n$ , the change in travel time  $\Delta t$   
 172 will remain the same. If we input tremor with these shifted Green's functions into the phase  
 173 coherence calculation in equation (3), we eliminate the travel time change and obtain

$$C_p^{com}(f) = \frac{1}{N} \sum_{k=1}^N \frac{2}{3(3-1)} \sum_{m=1}^3 \sum_{n=m+1}^3 \operatorname{Re} \left[ \frac{(\hat{s}_t \hat{g}_{km})(\hat{s}_d^* \hat{g}_{km}^* e^{-i2\pi f \Delta t})(\hat{s}_t^* \hat{g}_{kn})(\hat{s}_d \hat{g}_{kn} e^{i2\pi f \Delta t})}{|\hat{s}_t \hat{s}_d \hat{g}_{km} \hat{g}_{kn}|^2} \right] = 1. \quad (4)$$

174 Here  $s_t$  and  $s_d$  are the source time functions of the template and tremor signals, respectively.

175 It is of course difficult to know whether the Green's functions' shapes remain the same  
 176 over broad regions. We find empirically that the Green's functions retain a similar enough  
 177 shape for detection even as tremor locations change by 10 to 20 km; we obtain high  $C_p^{com}$   
 178 when the inter-station  $C_p^{sta}$  calculations for nearby templates imply that tremor is located  
 179 up to 10 or 20 km away from the template.

## 180 4. Templates, Data, and Processing

181 In our initial approach to the data, we compute the phase coherence  $C_p^{sta}$  and  $C_p^{com}$   
182 between each template and the seismic data recorded during 13 to 20 day-long intervals  
183 during four major slow slip events in 2004, 2008, 2009, and 2010. The 130 LFE templates  
184 created by Bostock et al. (2012) are located beneath the southern tip of Vancouver Island  
185 and the Juan de Fuca Strait, at depths ranging from 28 to 45 km (crosses in Figure 2).

186 We use data from stations in permanent and temporary seismic networks, including the  
187 Canadian National Seismograph Network (CN), the POLARIS-BC Network (PO; Nicholson  
188 et al., 2005), the Plate Boundary Observatory Borehole Seismic Network (PBO), the Pacific  
189 Northwest Seismic Network (UW), and the USArray Transportable Array (TA). The avail-  
190 able networks and stations evolved between the different slow slip events. Stations from the  
191 POLARIS-BC network were available only during the 2004 event while the PBO stations  
192 are available only after 2008. The POLARIS-BC network is ideal for this study, thanks to  
193 its dense configuration across the southern half of Vancouver Island, and Figure 2 shows  
194 the stations used for the 2004 slow slip event. Maps and tables of the 2008, 2009 and 2010  
195 networks are available in Figure S1 and Table T1.

196 To prepare the data, we filter the target and template seismograms to between 0.6 Hz and  
197 20 Hz and downsample to a common sampling rate of 40 Hz. We extract a portion of each  
198 template, from 0.2 s before to 4.8 s after a manually picked S-wave arrival and then compute  
199 the coherences  $C_p^{sta}$  and  $C_p^{com}$  between these template segments and a set of overlapping 60  
200 second-long windows of target data, starting every 6 s.

201 Further details of the  $C_p$  calculations are as described by Hawthorne and Ampuero (2017),  
202 but to summarise, we first cross-correlate at each station in the time domain, computing  
203  $d_{dkm} \cdot d_{tkm}$ . Then we taper the time domain correlation with a Hanning filter, convert to the  
204 frequency domain, compute  $C_p$ , and average  $C_p$  over frequencies between 1 and 6 Hz.

## 205 5. Observed Large-Scale Tremor Patterns

206 Figure 3 shows 10 days of  $C_p^{sta}$  and  $C_p^{com}$  during the 2004 slow slip event for two different  
207 templates (#246 and #12), about 40 km one from another. During the first days analyzed,  
208 tremor has not yet reached Vancouver Island. The calculated phase coherence is scattered  
209 around 0, and no high values stand out. The amplitude of the scatter in  $C_p$  depends on noise  
210 in the template used and on the number of available stations. With the stations available  
211 in 2004, standard deviations in  $C_p^{sta}$  are between 0.007 and 0.05, and standard deviations in  
212  $C_p^{com}$  are between 0.015 and 0.036.

213 When the main slow slip front reaches the locations of the templates, the coherence values  
214 begin to spike to values well above noise-induced variability. The templates in Figure 3 see  
215 the main front arrival on the 14<sup>th</sup> and 15<sup>th</sup> July, respectively, and have  $C_p^{com}$  values that reach  
216 0.38 and  $C_p^{sta}$  values that reach 0.17. However, the coherence values are not continuously  
217 high. The activity is fragmented into 1 to 30 minute-long spikes separated by intervals of low  
218 coherence that last minutes to hours. The spikes associated with the templates in Figure 3  
219 can be seen in more detail in the 8 hour-long windows in panels c and d, but similar spikes  
220 in coherence are observed for all 130 templates examined in this study. The most intense  
221 sequence of spikes typically lasts 1 to 2 days, while the main front passes, but spikes in

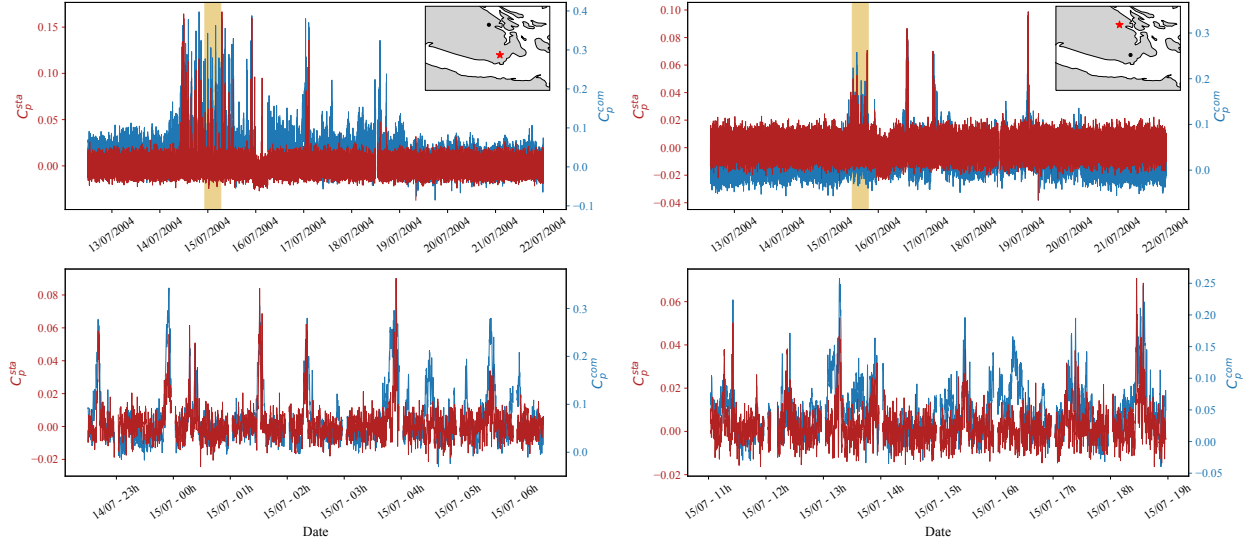


Figure 3: **Phase coherence time series for two templates in 2004.** **a-b)** 10 days-long time series of the inter-station phase coherence ( $C_p^{sta}$ , red) and the inter-component phase coherence ( $C_p^{com}$ , blue). The red star in each inset shows the location of the associated template. The orange bands delimit the time period shown in c-d. **c-d)** An expanded view of 8 hours of the time series shown in a) and b), respectively.

222 coherence can be seen for up to five days.

223 The spikes in the phase coherence  $C_p^{sta}$  and  $C_p^{com}$  are presumably created by bursts of  
 224 tremor occurring on the plate interface. The inter-component coherence  $C_p^{com}$  is ideal for  
 225 identifying and measuring the duration of these bursts, as  $C_p^{com}$  seems to remain high even  
 226 when tremor spreads to locations as far as 10 to 20 km from a given template. In contrast,  
 227 the inter-station coherence  $C_p^{sta}$  decreases when the tremor is offset by more than a fraction of  
 228 the seismic wavelength. The difference in inter-component and inter-station tremor detection  
 229 is apparent for a number of spikes for template #246 (Figure 3a and c). For instance, the  
 230 spike at 3:45 on the 15<sup>th</sup> July is longer on the  $C_p^{com}$  time series, and the spike at 4:30 on the  
 231 15<sup>th</sup> July is observable only the  $C_p^{com}$  time series.

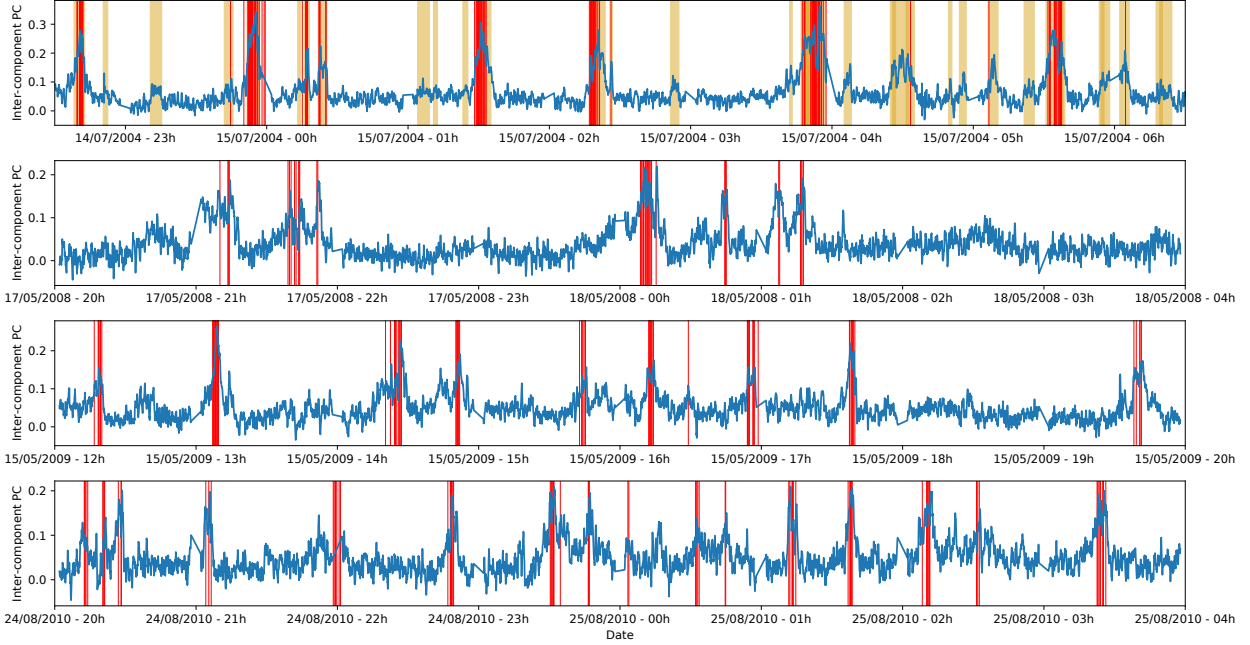


Figure 4:  $C_p^{com}$  over multiple slow slip events. Inter-component phase coherence  $C_p^{com}$  with template LFE #246, for time intervals in (a) 2004, (b) 2008, (c) 2009, and (d) 2010. Red lines mark the timing of LFE detections from (Bostock et al., 2015). Yellow bands on the top plot show identified spikes in the  $C_p^{com}$  time series, requiring that peaks are at least with  $\alpha = 3.0$  times the standard deviation.

232 We use a simple peak detection algorithm included in SciPy to identify a number of  
 233 spikes in each  $C_p^{com}$  time series. Proposed spikes are identified as maxima in  $C_p^{com}$  when

$$C_{p,k}^{comp} \geq \alpha \times \sigma_{C_{p,k}}, \quad (5)$$

234 where  $\sigma_{C_{p,k}}$  the standard deviation of the phase coherence during a time before tremor begins,  
 235 and  $\alpha$  is a factor between 2.0 and 3.5. The beginning and end of the spikes are the times  
 236 when  $C_p^{com}$  decreases to half its maximum value, and we accept spikes that last at least  
 237 60 seconds. Depending on the threshold  $\alpha$ , we detect between 22,000 and 86,000 events  
 238 in 2004. Several spikes are delineated in yellow in Figure 4a. Catalogues of the spikes are  
 239 provided as a supplementary file, and Figure S7 shows the distribution of spike durations



240 for different values of  $\alpha$ . Note that because we use a 60-second window for our coherence  
241 calculations,  $C_p^{com}$  is smoothed on that timescale, and the durations of shorter spikes may  
242 be overestimated.

243 Figure 2 shows the spatio-temporal distribution of tremor bursts detected with  $\alpha = 3.0$ .  
244 Each burst is plotted at a random location within 5 km of the associated template location  
245 and are colored by time. The bursts track the along-strike propagation of the main ETS  
246 front in 2004, from the Juan de Fuca Strait on the 10<sup>th</sup> July to  $\sim 90$  km northwest of the  
247 Strain on the 19<sup>th</sup> July (e.g., Wech et al., 2009; Bostock et al., 2015).

248 We can also compare our results directly with the LFE detections of Bostock et al. (2015).  
249 Vertical red lines in Figure 4 mark LFE detections with the relevant template. The matched  
250 filter detections in the catalogue coincide remarkably well with times of high phase coherence.  
251 All LFE detections occur within intervals of high  $C_p^{com}$ , though a few intervals of high  $C_p^{com}$   
252 do not include a LFE detection. The lack of LFE detections in some high  $C_p^{com}$  intervals  
253 may arise because tremor is coming from an adjacent part of the fault or because the tremor  
254 time series is complex, so that it is difficult to separate overlapping LFEs with a matched  
255 filter approach.

256 We observe similar tremor burst spacing and migration patterns for the 2008, 2009, and  
257 2010 slow slip events (Figure S1). 8 hour-long  $C_p^{com}$  time series from the four events can be  
258 compared in Figure 4, though we focus on the 2004 results in this study because the  $C_p$  time  
259 series have the highest resolution in 2004, when the POLARIS seismic network was running  
260 on Vancouver Island.

## 261 6. Tremor Burst Propagation

### 262 6.1. One Example

263 Our observed spikes in  $C_p^{com}$ , along with tremor spikes seen in previous work (Ghosh  
264 et al., 2009; Rubin and Armbruster, 2013; Bostock et al., 2015), suggest that much of the  
265 tremor in Cascadia occurs in short bursts. Here we seek to probe the bursts in more detail:  
266 to examine the shape and migration some of the shorter bursts.

267 We track the spatial and temporal evolution of 17 tremor bursts that are visible as well-  
268 resolved spikes in the  $C_p^{com}$  record. We identify a high-quality template that records each  
269 burst and then define a circular grid of potential tremor locations around that template, as  
270 illustrated in Figure 5a. Each grid is 8 km in diameter and is inclined along the slab interface  
271 identified by McCrory et al. (2012). In order to track tremor within the grid, we note that  
272 tremor coming from each of the possible locations is likely to have a Green’s function whose  
273 shape is similar to the template’s Green’s function. We verify that similarity by comparing  
274 the waveforms of closely spaced template LFEs; the waveforms of templates located about  
275 5 km apart have similar shapes (see Figure S2).

276 We shift the timing of the template seismograms to reflect the variation in the source-  
277 station travel time among the grid locations. The travel time for each location is computed  
278 using a uniform shear wave velocity model. We have estimated the apparent shear wave  
279 velocity for each LFE template by plotting the variation in 3-D distance from the LFE to  
280 the various stations against the arrival time for each station. We observe a linear relationship  
281 between distance and travel time, suggesting that a uniform velocity model is sufficient for

282 our analysis. Tests with a layered velocity model and ray path calculations achieved similar  
283 results.

284 Once we have time-shifted the template waveforms for a given location, we compute  
285 the inter-station phase coherence  $C_p^{sta}$  to determine when tremor occurs at that location.  
286 Figure 5 shows snapshots of the coherence during one three minute-long burst. During this  
287 time, the region of high phase coherence migrates about 1.6 km at a speed around 30 km/hr.  
288 The tremor moves from southeast to northwest, roughly along the strike of the subduction  
289 zone. This northwestward migration is pulse-like; the first location stops generating tremor  
290 before the last location generates tremor.

## 291 *6.2. Propagation for 17 Tremor Bursts*

292 Tremor migration is also well-resolved for 16 other analysed bursts, with migration du-  
293 rations between 60 and 1100 seconds. Some of these are illustrated in flipbooks M1 to M7  
294 in the supplementary material. To more precisely characterise the tremor migration speed  
295 in each burst, we select a profile across the grid parallel to its propagation direction and  
296 identify the front position (Figure S4). We then compute a linear regression between the  
297 propagating front position and time to obtain the propagation velocity (Figure S5). The 17  
298 analysed bursts and their propagation speeds are listed in Table T2. Figure 1a shows the  
299 relationship between the bursts' duration  $T$  and the propagation velocity  $V_r$  of the 17 events.

300 We cannot be sure that the observed duration-propagation velocity relationship is repre-  
301 sentative of the general population of tremor bursts, as we did not choose the bursts to be  
302 analysed in a systematic way. We determined tremor location in several tens of bursts with

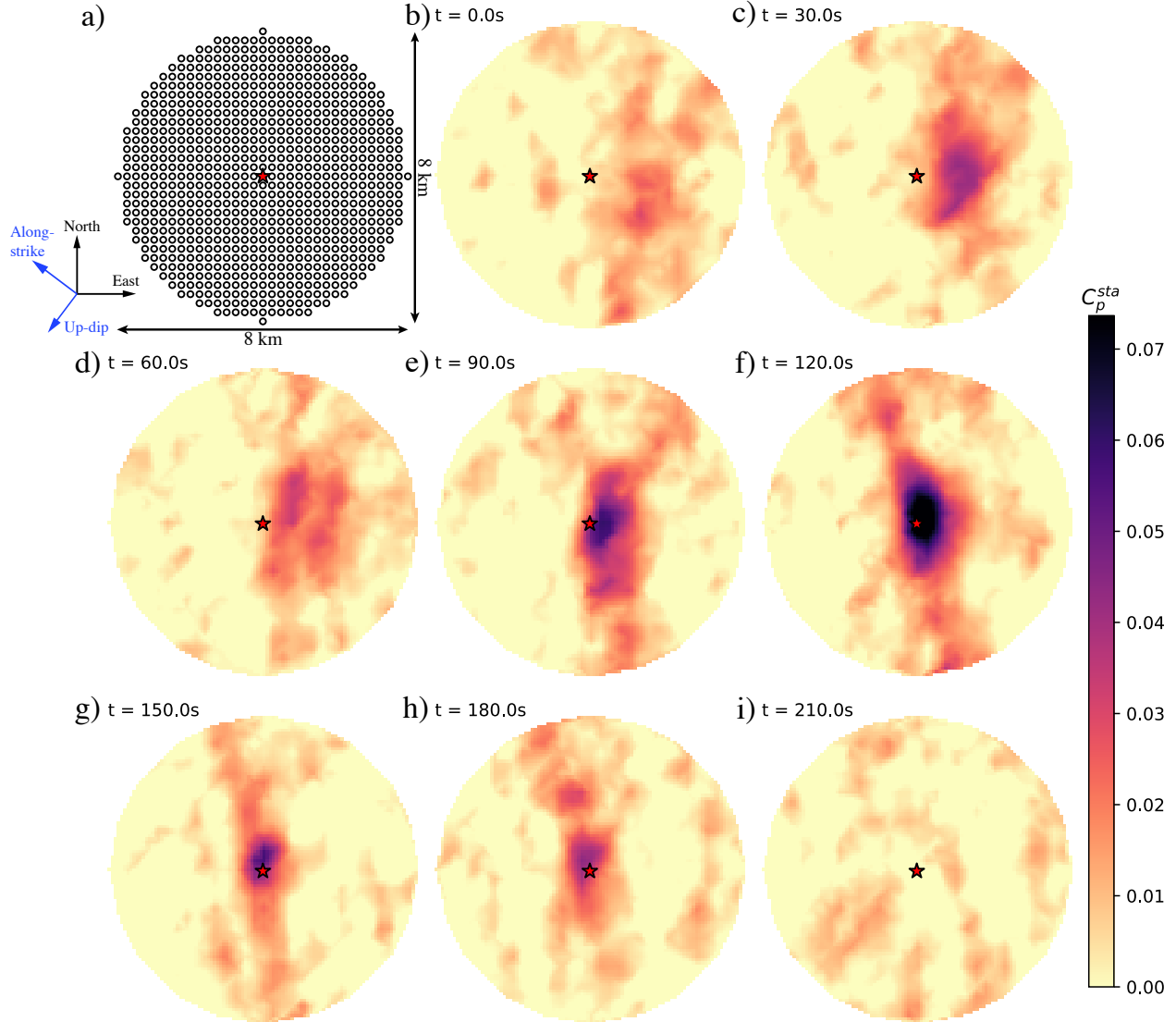


Figure 5: **Grid search for tremor during a burst detected at template #181.** a) Grid configuration and dimensions. b-i) Snapshots of  $C_p^{sta}$  computed for each point on the grid shown in a and interpolated. Indicated times are the middle of one-minute-long window used to compute the phase coherence. Red stars mark the location of the LFE used as template. In this example, the slow-slip propagates roughly 1.6 km at 9.2 m/s.

303 high  $C_p^{com}$  values and identified those with clear migration Nevertheless, it is interesting to  
 304 note that among the 17 events analysed, shorter events propagate faster. The minute-long

305 events propagates at more than 20 m/s, while the 15 minute-long events propagate at only  
306  $\sim 4$  m/s.

307 The faster propagation of shorter bursts persists for two definitions of burst duration.  
308 The open squares in Figure 1a indicate the durations of visually identified tremor migration  
309 while the the filled circles indicate durations estimated from the  $C_p^{com}$  time series: when  
310  $C_p^{com}$  is above a local background value. This latter definition of duration is likely to be  
311 more accurate, as the tremor could migrate out of the 8-km grid where we computed  $C_p^{sta}$ ,  
312 and the inter-component phase coherence  $C_p^{com}$  can identify at least some tremor in a broader  
313 region.

### 314 *6.3. Range of Observable Propagation Velocities*

315 Before we interpret the observed durations and propagation velocities, however, it is  
316 important to note that we have chosen our methodology to examine a particular range of  
317 tremor bursts: those with durations between 1 and 30 minutes and propagation extents  
318 between 1 and 8 km. This range of observable speeds and durations is outlined with a  
319 dashed line in Figure 1a.

320 We cannot identify migration over distances less than 1 km because of the resolution of  
321 the phase coherence calculations given 1-6 Hz seismic data from 5 to 10 stations. To map the  
322 potential smearing of the high coherence region for a given template, we create a synthetic  
323 signal for each point on the circular grid by time-shifting the template waveforms. Then we  
324 compute  $C_p^{sta}$  between those synthetics and the unshifted template seismograms. Some of  
325 the noisier template seismograms allow for elongate smearing of the high  $C_p^{sta}$  over 3 km-long

326 distances (Figure S3c and d). However, we have looked for tremor propagation only with the  
327 higher-quality templates, which show relatively circular smearing of high  $C_p^{sta}$  over smaller  
328 regions, with half-width of around 0.5 km (Figure S3a and b). These resolution tests imply  
329 that we should be able to identify tremor that propagates around 1 km or more.

330 We cannot identify migration over distances larger 8 km because that migration would  
331 extend outside the 8 km-wide grid around the relevant template LFEs, and we have not de-  
332 veloped the technique to map migration from the area around one LFE template to another.  
333 This 8-km limit constrains the open squares to fall below the upper diagonal dashed line in  
334 Figure 1a. However, synthetic tests imply if there were rapid propagation in larger events,  
335 we could have identified at least a few km of that propagation (Figure S6). And the filled  
336 circles can in principle plot up to a factor of 2 above the 8-km line, as they indicate durations  
337 taken from spikes in the  $C_p^{com}$  record. Comparisons of  $C_p^{com}$  and  $C_p^{sta}$  suggest that  $C_p^{com}$  can  
338 remain high when tremor is within 10 or 20 km of the template.

339 The roughly 1 to 8 km constraints suggest that we would observe an anticorrelation  
340 between burst duration and propagation speed even for a collection of bursts with random  
341 properties. However, the durations and propagation speeds we observe do not seem to fill  
342 the box of observable values; they are more consistent with the  $T^{-1/2}$  trend that one would  
343 expect for slow earthquakes whose moments scale linearly with duration. It thus seems  
344 likely that our observed duration-propagation speed anticorrelation is real—not entirely an  
345 observational artefact, but since we did not choose the 17 bursts to analyse rigorously, we  
346 cannot be sure.

## 347 7. Discussion

348 We have used a high-precision, coherence-based technique to identify numerous bursts of  
349 tremor. We mapped tremor migration over 1 to 6 km in 17 bursts with durations between  
350 1 and 22 minutes. The tremor migrates at speeds of 4 to 20 m/s, moving more quickly in  
351 shorter bursts. The sub-ten minute, rapidly migrating bursts represent a new observation.  
352 They are yet another category of slow earthquakes that must be reproduced by any complete  
353 physical model of subduction zone slip.

### 354 7.1. *Pulse-Like Ruptures*

355 If we assume, as seems plausible, that the observed migration of tremor results from a  
356 migrating location of aseismic slip, it is interesting to note that the propagation of tremor  
357 is pulse-like rather than crack-like; the locations slipping early in the bursts (e.g., brighter  
358 portions of Figure 5b and c) stop slipping before slip occurs at later locations (e.g., in  
359 Figure 5g and h). Such pulse-like migration of tremor and slip is also apparent in the main  
360 slow slip events in Cascadia, as well as in some longer tremor bursts (Dragert et al., 2001;  
361 Wech et al., 2009; Ghosh et al., 2010; Royer et al., 2015).

362 Pulse-like ruptures can appear unintuitive because slip at later locations should increase  
363 the stress at the initial locations, and that stress increase has the potential to drive slip. The  
364 pulse-like ruptures could indicate that the slow slip region has a particular type of rheology:  
365 one that allows a rapid recovery in stress as the slip rate slows, so that the initial location can  
366 accommodate an increasing stress as it slows down but other parts of the fault accelerate  
367 (Heaton, 1990; Zheng and Rice, 1998; Lu et al., 2007; Noda et al., 2009; Bizzarri, 2010).

368 Alternatively, the pulse-like ruptures could indicate that the subevent rupture is constrained  
369 to an elongate region. Slip may migrate along the long axis of that region, and the initial  
370 slipping location may stop slipping because it has slipped enough relative to its short-axis  
371 edges to accommodate the local stress drop. Slip at the far end of the rupture may produce  
372 an insignificant stress change at the initial location (e.g., Hawthorne and Rubin, 2013a;  
373 Michel et al., 2017; Dal Zilio et al., 2020).

374 However, pulse-like ruptures are unlikely in some models of slow slip. One of the first  
375 proposed explanations of slow slip suggests that slow slip regions have a "standard," po-  
376 tentially unstable, velocity-weakening rheology but that the regions have a particular size;  
377 they may be large enough to accelerate but too small to reach seismic slip speeds (Liu and  
378 Rice, 2005, 2007; Rubin, 2008; Li et al., 2018; Romanet et al., 2018). But most simulations  
379 of those size-limited slow slip ruptures appear more crack-like than pulse-like, at least in a  
380 visual inspection (Liu and Rice, 2005; Rubin, 2008). A more rigorous investigation of the slip  
381 rate profiles in these models would help us further assess whether fault sizes and geometry  
382 alone can explain slow slip events.

### 383 *7.2. Too Fast to Be Driven by a Change in Stress Drop?*

384 We may also investigate the rheology of the slow slip region by addressing their speed:  
385 how can 5-minute-long subevents propagate 200 times faster than the main slow slip front?  
386 Do the subevents have a greater driving stress drop and thus a larger strain energy release,  
387 or do they have a lower resistance to acceleration: a smaller fracture energy? To partially  
388 address this question, we may note that the strain energy released in an elongate rupture



389 normally scales as  $\Delta\tau^2 W$ : as the stress drop  $\Delta\tau$  squared times the rupture width  $W$  (e.g.,  
390 Lawn, 1993). This strain energy must equal the fracture energy dissipated by the rupture,  
391 which is a function of the rheology, the initial conditions, and the slip rate. Most of the  
392 complex rheologies proposed to explain slow slip have fracture energies that increase dra-  
393 matically as the slip rate increases. The strong increase in resistance with slip rate keeps  
394 the slip rates low. A factor of 200 increase in slip rate, as seems plausible for our fastest  
395 events, is likely to require at least a factor of 10 increase in fracture energy in a shear-induced  
396 dilatancy model (Liu et al., 2010; Segall et al., 2010) and at least a factor of 5 increase in  
397 fracture energy in a model with a velocity-strengthening transition (Hawthorne and Rubin,  
398 2013a,c). Our subevents have widths  $W$  at least factor of 10 narrower than the main slow  
399 slip region, so for their slip to supply such an increased fracture energy, they would need  
400 stress drops at least 7 times larger than the main event stress drop. We do not have stress  
401 drops estimates for our subevents, but geodetic and tremor count-based analyses for half-  
402 to few-hour events suggest that subevent stress drops are comparable to or smaller than the  
403 main event stress drop (Rubin and Armbruster, 2013; Hawthorne et al., 2016; Bletery et al.,  
404 2017).

405 Some modelers have produced locally high stress drops and slip rates by mixing unstable  
406 patches into a mostly stable slow slip region (Ariyoshi et al., 2009, 2012; Colella et al., 2012;  
407 Peng and Rubin, 2018; Luo and Liu, 2021). However, these patch-driven models have focused  
408 on slightly slow tremor fronts and have so far allowed propagation rates less than 10 to 50  
409 times faster than the main front (Ariyoshi et al., 2012; Colella et al., 2012; Peng and Rubin,

410 2018). It remains to be seen whether patch-driven models can allow the higher propagation  
411 rates seen here and observed by Ghosh et al. (2010), particularly in ruptures that are just a  
412 few km wide.

413 If they cannot, it may be worth considering whether the slow slip rheology varies with  
414 time, perhaps because the pore pressure changes, (Rubin, 2011; Peng and Rubin, 2017) or  
415 whether fault properties vary in space to allow locally reduced resistance to high slip rates  
416 and thus faster ruptures.

### 417 *7.3. Potential Consistency With a Slow Earthquake Continuum*

418 It would be particularly interesting to consider spatially variable fault properties if we  
419 knew that a single fault zone process produced the entire range of slow earthquakes, from  
420 slow slip events to tremor LFEs (Ide et al., 2007). Some rheologies proposed to explain slow  
421 slip are unlikely to produce very wide-ranging slip rates, particularly if slip speeds increase  
422 as ruptures get smaller. For instance, a rheology where slip rate depends on temperature  
423 rather than patch size is unlikely to allow slip rates that increase by a factor of 10,000 as  
424 patches get smaller (Shibazaki and Iio, 2003; Matsuzawa et al., 2010; Hawthorne and Rubin,  
425 2013c). Size-limited models, where slip rates tend to be 10 to 100 times the driving slip rate  
426 (Liu and Rice, 2005, 2007; Rubin, 2008; Skarbek et al., 2012; Wei et al., 2018), may also be  
427 unlikely to produce very high slip rates. The apparently faster slip in smaller events could  
428 indicate that whatever process generates slip in slow earthquakes, it depends on some size-  
429 dependent fault property. For instance, fault zone width might be smaller on smaller fault  
430 segments, allowing shorter fluid diffusion times and faster slip in dilatancy models (Marone

431 et al., 1990; Lockner and Byerlee, 1994; Segall and Rice, 1995; Segall et al., 2010; Liu et al.,  
432 2010; Liu, 2013), or smaller patches could have high concentrations of brittle asperities that  
433 drive rapid viscous deformation (Lavie et al., 2013; Fagereng et al., 2014; Behr et al., 2018;  
434 Goswami and Barbot, 2018; Behr and Brgmann, 2021).

435 A range of observations have suggested that we should consider these size-dependent  
436 fault properties. Smaller observed slow earthquakes tend to be faster (see Figure 1 and e.g.,  
437 Ide et al., 2007; Gao et al., 2012), and the statistics of observed slip are consistent with a  
438 continuum of slip rates (Ide, 2008; Ide and Maury, 2018; Hawthorne and Bartlow, 2018).

439 Our identified subevents results may provide further evidence that slow earthquakes  
440 constitute a continuum with size-dependent slip rates. We find that smaller tremor bursts  
441 are faster, and our observed propagation velocities and durations fall along the trends defined  
442 by previously observed slow earthquakes, as shown in Figure 1b. The match with previous  
443 observations is not perfect, but the mismatch could result from observational bias in tremor  
444 detection. Our results are restricted by the methodology to a size range between 1 and  
445 8 km, and some others' results are also restricted. The RTRs and slow slip fronts identified  
446 by Houston et al. (2011) and Bletery et al. (2017) are constrained to be longer than 10 km  
447 because they used tremor with location spacing or accuracy of 5 to 10 km.

448 Our propagation rates are difficult to directly compare with the linear moment-duration  
449 scaling found by Ide et al. (2007). However, we can roughly compare the two by plotting  
450 black lines in each panel of Figure 1, which assume that (1) slow earthquake moments scale  
451 linearly with duration, with a moment rate of  $3 \times 10^{12}$  N m s<sup>-1</sup>, and (2) slow earthquakes

452 have magnitude-independent stress drops  $\Delta\tau$  around 30 kPa, as is consistent with a few ob-  
453 servations but remains poorly constrained (Schmidt and Gao, 2010; Rubin and Armbruster,  
454 2013; Hawthorne et al., 2016; Bletery et al., 2017; Chestler and Creager, 2017; Thomas et al.,  
455 2018). We assume elliptical ruptures with uniform stress drop and a 3:1 aspect ratio, and  
456 we estimate the propagation velocity by dividing the length of the ellipse by the rupture  
457 duration. The comparison suggests that our propagation rates also fall roughly along the  
458 trend defined by observed slow earthquakes’ moments and durations.

#### 459 *7.4. Potential Inconsistency With a Slow Earthquake Continuum*

460 However, it is too early to firmly infer that all slow earthquakes are governed by the  
461 same fault zone processes. Our results fill one observational gap, but other gaps in the slow  
462 earthquake spectrum remain, and we have not addressed observed scalings that differ from  
463 the overall trend in Figure 1c (Bostock et al., 2015; Gomberg et al., 2016; Michel et al., 2019;  
464 Farge et al., 2020; Supino et al., 2020).

465 Further, one could interpret our observed propagation velocities as evidence against a  
466 simple continuum of slow earthquakes. The events we analyse are slightly slower than one  
467 would expect after extrapolating the propagation velocities of tremor fronts identified by  
468 Bletery et al. (2017) and (Houston et al., 2011) (Figure 1b). One could argue that there are  
469 slow earthquakes with a wide range of propagation rates and durations, located all over the  
470 plot in Figure 1b. Our and others’ identified events could simply have sizes that reflect our  
471 observational capabilities (Gomberg et al., 2016).

472 Such observational bias does not seem to explain all the trends in the observed events’

473 sizes. For instance, by extracting durations from the  $C_p$  time series and propagation from  
474 the tremor locations, we should be able to identify at least part of the propagation in longer,  
475 faster events, even if they are 20 km across. And if 30-s-long  $M_W$  5 earthquakes were  
476 common, it would be surprising that they have not yet been spotted. But it may also be  
477 surprising, at least to our physical intuition, that a single fault zone process could create  
478 slow earthquakes with wide-ranging slip rates, so we must be careful to remember that many  
479 events could go unobserved.

## 480 8. Conclusions

481 We have identified thousands of short bursts of tremor beneath Vancouver Island by  
482 employing a phase coherence method developed by Hawthorne and Ampuero (2017) and  
483 set of template LFE waveforms created by Bostock et al. (2012). For seventeen bursts, we  
484 perform a grid search on the fault plane to track the evolution of tremor and likely slip.  
485 We find that these minutes-long events have pulse-like ruptures. They move 1 to 6 km at  
486 speeds of 3 m/s to 25 m/s. Smaller events tend to be faster, and the events' properties fall  
487 roughly, though not quite on, the duration-propagation velocity trend defined by previously  
488 observed events. These trends provide further, albeit still inconclusive, evidence that slow  
489 earthquakes with a wide range of slip rates are created by the same fault zone processes.  
490 In any case, they indicate that any complete physical model of slow slip in Cascadia should  
491 reproduce not just events that last weeks, with propagation rates of 0.1 m/s, and subevents  
492 that last 3 hours, with propagation rates of 5 m/s, but also subevents that last 2 minutes,  
493 with propagation rates of 20 m/s.

## 494 **9. Data availability**

495 The tremor catalogues created in this study are in the process of being uploaded to a  
496 National Geoscience Data Centre repository, hosted by the British Geological Survey. The  
497 catalogues are temporarily available at  
498 [https://drive.google.com/drive/folders/1HhDKhwU\\_dfymJR01tgTJMYXE0GdI03pu?usp=sharing](https://drive.google.com/drive/folders/1HhDKhwU_dfymJR01tgTJMYXE0GdI03pu?usp=sharing).

## 499 **10. Acknowledgements**

500 We thank M. Bostock for providing the LFE catalogue and waveforms and J. Cassidy for  
501 his help with missing data during the 2008 ETS. The facilities of IRIS Data Services, and  
502 specifically the IRIS Data Management Center, were used for access to waveforms, related  
503 metadata, and/or derived products used in this study. IRIS Data Services are funded through  
504 the Seismological Facilities for the Advancement of Geoscience and EarthScope (SAGE)  
505 Proposal of the National Science Foundation under Cooperative Agreement EAR-1261681.  
506 This study was funded by NERC standard grant NE/P012507/1.

## 507 **References**

- 508 Ariyoshi, K., Hori, T., Ampuero, J.P., Kaneda, Y., Matsuzawa, T., Hino, R., Hasegawa,  
509 A., 2009. Influence of interaction between small asperities on various types of slow earth-  
510 quakes in a 3-D simulation for a subduction plate boundary. *Gondwana Res.* 16, 534–544.  
511 doi:10.1016/j.gr.2009.03.006.
- 512 Ariyoshi, K., Matsuzawa, T., Ampuero, J.P., Nakata, R., Hori, T., Kaneda, Y., Hino, R.,  
513 Hasegawa, A., 2012. Migration process of very low-frequency events based on a chain-

514 reaction model and its application to the detection of preseismic slip for megathrust  
515 earthquakes. *Earth Planets Space* 64, 693–702. doi:10.5047/eps.2010.09.003.

516 Armbruster, J.G., Kim, W.Y., Rubin, A.M., 2014. Accurate tremor locations from coherent  
517 S and P waves. *J. Geophys. Res.* 119, 5000–5013. doi:10.1002/2014JB011133.

518 Baba, S., Takeo, A., Obara, K., Matsuzawa, T., Maeda, T., 2020. Comprehensive detection of  
519 very low frequency earthquakes off the Hokkaido and Tohoku Pacific coasts, northeastern  
520 Japan. *J. Geophys. Res.* 125. doi:10.1029/2019JB017988.

521 Bartlow, N.M., Miyazaki, S., Bradley, A.M., Segall, P., 2011. Space-time correlation of slip  
522 and tremor during the 2009 Cascadia slow slip event. *Geophys. Res. Lett.* 38, L18309.  
523 doi:10.1029/2011GL048714.

524 Behr, W.M., Brgmann, R., 2021. Whats down there? The structures, materials and  
525 environment of deep-seated slow slip and tremor. *Philosophical Transactions of the*  
526 *Royal Society A: Mathematical, Physical and Engineering Sciences* 379, 20200218.  
527 doi:10.1098/rsta.2020.0218.

528 Behr, W.M., Kotowski, A.J., Ashley, K.T., 2018. Dehydration-induced rheological hetero-  
529 geneity and the deep tremor source in warm subduction zones. *Geology* 46, 475–478.  
530 doi:10.1130/G40105.1.

531 Bizzarri, A., 2010. Pulse-like dynamic earthquake rupture propagation under rate-  
532 , state- and temperature-dependent friction. *Geophys. Res. Lett.* 37, L18307.  
533 doi:201010.1029/2010GL044541.

534 Bletery, Q., Thomas, A.M., Hawthorne, J.C., Skarbek, R.M., Rempel, A.W., Krogstad,  
535 R.D., 2017. Characteristics of secondary slip fronts associated with slow earthquakes in  
536 Cascadia. *Earth Planet. Sci. Lett.* 463, 212–220. doi:10.1016/j.epsl.2017.01.046.

537 Bostock, M.G., Royer, A.A., Hearn, E.H., Peacock, S.M., 2012. Low frequency earth-  
538 quakes below southern Vancouver Island. *Geochem., Geophys., Geosyst.* 13, Q11007.  
539 doi:10.1029/2012GC004391.

540 Bostock, M.G., Thomas, A.M., Savard, G., Chuang, L., Rubin, A.M., 2015. Magnitudes  
541 and moment-duration scaling of low-frequency earthquakes beneath southern Vancouver  
542 Island. *J. Geophys. Res.* 120, 6329–6350. doi:10.1002/2015JB012195.

543 Brown, J.R., Beroza, G.C., Shelly, D.R., 2008. An autocorrelation method to de-  
544 tect low frequency earthquakes within tremor. *Geophys. Res. Lett.* 35, L16305.  
545 doi:10.1029/2008GL034560.

546 Bucker, H.P., 1976. Use of calculated sound fields and matchedfield detection to locate sound  
547 sources in shallow water. *J. Acoust. Soc. Amer.* 59, 368–373. doi:10.1121/1.380872.

548 Chestler, S.R., Creager, K.C., 2017. Evidence for a scale-limited low-frequency earthquake  
549 source process. *J. Geophys. Res.* 122, 3099–3114. doi:10.1002/2016JB013717.

550 Colella, H.V., Dieterich, J.H., Richards-Dinger, K., Rubin, A.M., 2012. Complex charac-  
551 teristics of slow slip events in subduction zones reproduced in multi-cycle simulations.  
552 *Geophys. Res. Lett.* 39, L20312. doi:10.1029/2012GL053276.



553 Corciulo, M., Roux, P., Campillo, M., Dubucq, D., Kuperman, W., 2012. Multiscale  
554 matched-field processing for noise-source localization in exploration geophysics. GEO-  
555 PHYSICS 77, KS33–KS41. doi:10.1190/geo2011-0438.1.

556 Cruz-Atienza, V.M., Villafuerte, C., Bhat, H.S., 2018. Rapid tremor migration and pore-  
557 pressure waves in subduction zones. Nat. Comm. 9. doi:10.1038/s41467-018-05150-3.

558 Dal Zilio, L., Lapusta, N., Avouac, J., 2020. Unraveling scaling properties of slowslip events.  
559 Geophys. Res. Lett. 47. doi:10.1029/2020GL087477.

560 Douglas, A., Beavan, J., Wallace, L., Townend, J., 2005. Slow slip on the northern Hikurangi  
561 subduction interface, New Zealand. Geophys. Res. Lett. 32, 16305.

562 Dragert, H., Wang, K.L., James, T.S., 2001. A silent slip event on the deeper Cascadia  
563 subduction interface. Science 292, 1525–1528. doi:10.1126/science.1060152.

564 Fagereng, ., Hillary, G.W.B., Diener, J.F.A., 2014. Brittle-viscous deformation, slow slip,  
565 and tremor. Geophys. Res. Lett. 41, 4159–4167. doi:10.1002/2014GL060433.

566 Farge, G., Shapiro, N.M., Frank, W.B., 2020. Moment-duration scal-  
567 ing of Low-Frequency Earthquakes in Guerrero, Mexico. J. Geo-  
568 phys. Res. n/a, 2019JB019099. doi:10.1029/2019JB019099. eprint:  
569 <https://agupubs.onlinelibrary.wiley.com/doi/pdf/10.1029/2019JB019099>.

570 Frank, W., 2016. Slow slip hidden in the noise: The intermittence of tectonic release.  
571 Geophys. Res. Lett. 43. doi:10.1002/2016GL069537.

572 Frank, W.B., Shapiro, N.M., Husker, A.L., Kostoglodov, V., Romanenko, A., Campillo, M.,  
573 2014. Using systematically characterized low-frequency earthquakes as a fault probe in  
574 Guerrero, Mexico. *J. Geophys. Res.* 119, 7686–7700. doi:10.1002/2014JB011457.

575 Gao, H., Schmidt, D.A., Weldon, R.J., 2012. Scaling relationships of source parameters for  
576 slow slip events. *Bull. Seis. Soc. Amer.* 102, 352–360. doi:10.1785/0120110096.

577 Geological Survey of Canada, 1989. Canadian National Seismograph Network. In-  
578 ternational Federation of Digital Seismograph Networks. Dataset / seismic network.  
579 doi:<https://doi.org/10.7914/SN/CN>.

580 Ghosh, A., Vidale, J.E., Sweet, J.R., Creager, K.C., Wech, A.G., 2009. Tremor patches  
581 in Cascadia revealed by seismic array analysis. *Geophys. Res. Lett.* 36, L17316.  
582 doi:10.1029/2009GL039080.

583 Ghosh, A., Vidale, J.E., Sweet, J.R., Creager, K.C., Wech, A.G., Houston, H., Brodsky,  
584 E.E., 2010. Rapid, continuous streaking of tremor in Cascadia. *Geochem., Geophys.,*  
585 *Geosyst.* 11, Q12010. doi:10.1029/2010GC003305.

586 Gomberg, J., Wech, A., Creager, K., Obara, K., Agnew, D., 2016. Reconsidering earthquake  
587 scaling. *Geophys. Res. Lett.* 43, 6243–6251. doi:10.1002/2016GL069967.

588 Goswami, A., Barbot, S., 2018. Slow-slip events in semi-brittle serpentinite fault zones.  
589 *Scientific Reports* 8, 6181. doi:10.1038/s41598-018-24637-z.

590 Harris, D.B., Kvaerna, T., 2010. Superresolution with seismic arrays using empirical

591 matched field processing. *Geophys. J. Intern.* 182, 1455–1477. doi:10.1111/j.1365-  
592 246X.2010.04684.x.

593 Hawthorne, J.C., Ampuero, J.P., 2017. A phase coherence approach to identifying co-located  
594 earthquakes and tremor. *Geophys. J. Intern.* 209, 623–642. doi:10.1093/gji/ggx012.

595 Hawthorne, J.C., Bartlow, N.M., 2018. Observing and modeling the spectrum of a slow slip  
596 event. *J. Geophys. Res.* 123, 4243–4265. doi:10.1029/2017JB015124.

597 Hawthorne, J.C., Bostock, M.G., Royer, A.A., Thomas, A.M., 2016. Variations in slow slip  
598 moment rate associated with rapid tremor reversals in Cascadia. *Geochem., Geophys.,  
599 Geosyst.* 17, 4899–4919. doi:10.1002/2016GC006489.

600 Hawthorne, J.C., Rubin, A.M., 2013a. Laterally propagating slow slip events in a rate and  
601 state friction model with a velocity-weakening to velocity-strengthening transition. *J.  
602 Geophys. Res.* 118, 3785–3808. doi:10.1002/jgrb.50261.

603 Hawthorne, J.C., Rubin, A.M., 2013b. Short-time scale correlation between slow slip and  
604 tremor in Cascadia. *J. Geophys. Res.* 118, 1316–1329. doi:10.1002/jgrb.50103.

605 Hawthorne, J.C., Rubin, A.M., 2013c. Tidal modulation and back-propagating fronts in slow  
606 slip events simulated with a velocity-weakening to velocity-strengthening friction law. *J.  
607 Geophys. Res.* 118, 1216–1239. doi:10.1002/jgrb.50107.

608 Hawthorne, J.C., Thomas, A.M., Ampuero, J.P., 2019. The rupture extent of low frequency  
609 earthquakes near Parkfield, CA. *Geophys. J. Intern.* doi:10.1093/gji/ggy429.

610 Heaton, T.H., 1990. Evidence for and implications of self-healing pulses of slip in earth-  
611 quake rupture. *Physics of the Earth and Planetary Interiors* 64, 1–20. doi:10.1016/0031-  
612 9201(90)90002-F.

613 Houston, H., Delbridge, B.G., Wech, A.G., Creager, K.C., 2011. Rapid tremor rever-  
614 sals in Cascadia generated by a weakened plate interface. *Nat. Geosci.* 4, 404–409.  
615 doi:10.1038/ngeo1157.

616 Hutchison, A.A., Ghosh, A., 2016. Very low frequency earthquakes spatiotemporally asyn-  
617 chronous with strong tremor during the 2014 episodic tremor and slip event in Cascadia.  
618 *Geophys. Res. Lett.* 43, 6876–6882. doi:10.1002/2016GL069750.

619 Ide, S., 2008. A Brownian walk model for slow earthquakes. *Geophys. Res. Lett.* 35, L17301.  
620 doi:10.1029/2008GL034821.

621 Ide, S., 2010a. Quantifying the time function of nonvolcanic tremor based on a stochastic  
622 model. *J. Geophys. Res.* 115, B08313. doi:10.1029/2009JB000829.

623 Ide, S., 2010b. Striations, duration, migration and tidal response in deep tremor. *Nature*  
624 466, 356–359. doi:10.1038/nature09251.

625 Ide, S., Beroza, G.C., Shelly, D.R., Uchide, T., 2007. A scaling law for slow earthquakes.  
626 *Nature* 447, 76–79. doi:10.1038/nature05780.

627 Ide, S., Imanishi, K., Yoshida, Y., Beroza, G.C., Shelly, D.R., 2008. Bridging the gap between  
628 seismically and geodetically detected slow earthquakes. *Geophys. Res. Lett.* 35, L10305.  
629 doi:10.1029/2008GL034014.

630 Ide, S., Maury, J., 2018. Seismic moment, seismic energy, and source duration of slow  
631 earthquakes: Application of brownian slow earthquake model to three major subduction  
632 zones. *Geophys. Res. Lett.* 45, 3059–3067. doi:10.1002/2018GL077461.

633 IRIS Transportable Array, 2003. USArray transportable array. International  
634 Federation of Digital Seismograph Networks. Dataset / seismic network.  
635 doi:<https://doi.org/10.7914/SN/TA>.

636 Itaba, S., Ando, R., 2011. A slow slip event triggered by teleseismic surface waves. *Geophys.*  
637 *Res. Lett.* 38, L21306. doi:10.1029/2011GL049593.

638 Itaba, S., Kitagawa, Y., Koizumi, N., Takahashi, H., Matsumoto, N., Takeda, N., Kimura,  
639 H., Kimura, T., Matzuzawa, T., Shiomi, K., 2013. Short-term slow slip events in the Tokai  
640 area, the Kii Peninsula and the Shikoku District, Japan (from November 2012 to April  
641 2013). Report of the Coordinating Committee for Earthquake Prediction 90.

642 Ito, Y., Obara, K., 2006. Very low frequency earthquakes within accretionary prisms are very  
643 low stress-drop earthquakes. *Geophys. Res. Lett.* 33, L09302. doi:10.1029/2006GL025883.

644 Ito, Y., Obara, K., Shiomi, K., Sekine, S., Hirose, H., 2007. Slow earthquakes coincident with  
645 episodic tremors and slow slip events. *Science* 315, 503–506. doi:10.1126/science.1134454.

646 Kaneko, L., Satoshi, I., Nakano, M., 2018. Slow earthquakes in the microseism fre-  
647 quency band (0.11.0 hz) off Kii Peninsula, Japan. *Geophys. Res. Lett.* 45, 2618–2624.  
648 doi:10.1002/2017GL076773.

649 Kao, H., Shan, S.J., Dragert, H., Rogers, G., Cassidy, J.F., Wang, K., James, T.S., Ra-  
650 machandran, K., 2006. Spatial-temporal patterns of seismic tremors in northern Cascadia.  
651 J. Geophys. Res. 111, B03309. doi:10.1029/2005JB003727.

652 Kitagawa, Y., Itaba, S., Koizumi, N., Takahashi, M., Matsumoto, N., Takeda, N., 2011. The  
653 variation of the strain, tilt and groundwater level in the Shikoku District and Kii Peninsula,  
654 Japan (from November 2010 to May 2011). Report of the Coordinating Committee for  
655 Earthquake Prediction 86.

656 Kostoglodov, V., Singh, S.K., Santiago, J.A., Franco, S.I., Larson, K.M., Lowry, A.R.,  
657 Bilham, R., 2003. A large silent earthquake in the Guerrero seismic gap, Mexico. Geophys.  
658 Res. Lett. 30, 1807. doi:10.1029/2003GL017219.

659 Lavier, L.L., Bennett, R.A., Duddu, R., 2013. Creep events at the brittle ductile transition.  
660 Geochem., Geophys., Geosyst. 14, 3334–3351. doi:10.1002/ggge.20178.

661 Lawn, B., 1993. Fracture of Brittle Solids. 2 ed., Cambridge University Press, Cambridge, UK.

662 Li, H., Wei, M., Li, D., Liu, Y., Kim, Y., Zhou, S., 2018. Segmentation of slow slip events  
663 in south central Alaska possibly controlled by a subducted oceanic plateau. J. Geophys.  
664 Res. 123, 2017JB014911. doi:10.1002/2017JB014911.

665 Liu, L., Gurnis, M., Seton, M., Saleeby, J., Muller, R.D., Jackson, J.M., 2010. The  
666 role of oceanic plateau subduction in the Laramide orogeny. Nat. Geosci. 3, 353–357.  
667 doi:10.1038/ngeo829.

668 Liu, Y., 2013. Numerical simulations on megathrust rupture stabilized under strong  
669 dilatancy strengthening in slow slip region. *Geophys. Res. Lett.* 40, 1311–1316.  
670 doi:10.1002/grl.50298.

671 Liu, Y.J., Rice, J.R., 2005. Aseismic slip transients emerge spontaneously in three-  
672 dimensional rate and state modeling of subduction earthquake sequences. *J. Geophys.*  
673 *Res.* 110, B08307. doi:10.1029/2004JB003424.

674 Liu, Y.J., Rice, J.R., 2007. Spontaneous and triggered aseismic deformation transients in a  
675 subduction fault model. *J. Geophys. Res.* 112, B09404. doi:10.1029/2007JB004930.

676 Lockner, D.A., Byerlee, J.D., 1994. Dilatancy in hydraulically isolated faults and the sup-  
677 pression of instability. *J. Geophys. Res.* 21, 2353–2356. doi:10.1029/94GL02366.

678 Lu, X., Lapusta, N., Rosakis, A.J., 2007. Pulse-like and crack-like ruptures in experiments  
679 mimicking crustal earthquakes. *Proceedings of the National Academy of Sciences* 104,  
680 18931–18936. doi:10.1073/pnas.0704268104.

681 Luo, Y., Ampuero, J.P., 2017. Tremor migration patterns and the collective behavior of deep  
682 asperities mediated by creep. *EarthArXiv* doi:10.17605/OSF.IO/MBCAV.

683 Luo, Y., Liu, Z., 2021. Fault zone heterogeneities explain depth-dependent pattern and  
684 evolution of slow earthquakes in Cascadia. *Nat. Comm.* 12, 1959. doi:10.1038/s41467-021-  
685 22232-x.

686 Marone, C., Raleigh, C.B., Scholz, C.H., 1990. Frictional behavior and constitutive modeling  
687 of simulated fault gouge. *J. Geophys. Res.* 95, 7007–7025. doi:10.1029/JB095iB05p07007.

688 Masuda, K., Ide, S., Ohta, K., Matsuzawa, T., 2020. Bridging the gap between low-frequency  
689 and very-low-frequency earthquakes. *Earth, Planet. Space* 72, 47. doi:10.1186/s40623-020-  
690 01172-8.

691 Matsuzawa, T., Hirose, H., Shibazaki, B., Obara, K., 2010. Modeling short- and long-term  
692 slow slip events in the seismic cycles of large subduction earthquakes. *J. Geophys. Res.*  
693 115, B12301. doi:10.1029/2010JB007566.

694 Matsuzawa, T., Obara, K., Maeda, T., 2009. Source duration of deep very low fre-  
695 quency earthquakes in western Shikoku, Japan. *J. Geophys. Res.* 114, B00A11.  
696 doi:10.1029/2008JB006044.

697 Maury, J., Ide, S., Cruz-Atienza, V.M., Kostoglodov, V., Gonzalez-Molina, G., Prez-Campos,  
698 X., 2016. Comparative study of tectonic tremor locations: Characterization of slow earth-  
699 quakes in Guerrero, Mexico. *J. Geophys. Res.* 121, 5136–5151. doi:10.1002/2016JB013027.

700 McCrory, P.A., Blair, J.L., Waldhauser, F., Oppenheimer, D.H., 2012. Juan de Fuca slab  
701 geometry and its relation to Wadati-Benioff zone seismicity. *J. Geophys. Res.* 117, B09306.  
702 doi:10.1029/2012JB009407.

703 Michel, S., Avouac, J.P., Lapusta, N., Jiang, J., 2017. Pulse-like partial ruptures and high-  
704 frequency radiation at creeping-locked transition during megathrust earthquakes. *Geo-*  
705 *phys. Res. Lett.* 44. doi:10.1002/2017GL074725.

706 Michel, S., Gualandi, A., Avouac, J.P., 2019. Similar scaling laws for earthquakes and  
707 Cascadia slow-slip events. *Nature* 574, 522–526. doi:10.1038/s41586-019-1673-6.



708 Miller, M.M., Melbourne, T., Johnson, D.J., Sumner, W.Q., 2002. Periodic slow earthquakes  
709 from the Cascadia subduction zone. *Science* 295, 2423–2423. doi:10.1126/science.1071193.

710 Nicholson, T., Bostock, M., Cassidy, J.F., 2005. New constraints on subduction zone  
711 structure in northern Cascadia. *Geophys. J. Intern.* 161, 849–859. doi:10.1111/j.1365-  
712 246X.2005.02605.x.

713 Noda, H., Dunham, E.M., Rice, J.R., 2009. Earthquake ruptures with thermal weakening  
714 and the operation of major faults at low overall stress levels. *J. Geophys. Res.* 114, B07302.  
715 doi:10.1029/2008JB006143.

716 Obara, K., 2002. Nonvolcanic deep tremor associated with subduction in southwest Japan.  
717 *Science* 296, 1679–1681. doi:10.1126/science.1070378.

718 Obara, K., 2010. Phenomenology of deep slow earthquake family in southwest Japan:  
719 Spatiotemporal characteristics and segmentation. *J. Geophys. Res.* 115, B00A25.  
720 doi:10.1029/2008JB006048.

721 Obara, K., 2012. Depth-dependent mode of tremor migration beneath Kii Peninsula, Nankai  
722 subduction zone. *Geophys. Res. Lett.* doi:10.1029/2012GL051420.

723 Obara, K., Hirose, H., Yamamizu, F., Kasahara, K., 2004. Episodic slow slip events accom-  
724 panied by non-volcanic tremors in southwest Japan subduction zone. *Geophys. Res. Lett.*  
725 31, L23602. doi:10.1029/2004GL020848.

726 Obara, K., Sekine, S., 2009. Characteristic activity and migration of episodic tremor and  
727 slow-slip events in central Japan. *Earth Planets and Space* 61, 853–862.

728 Ochi, T., Itaba, S., Koizumi, N., Takahashi, M., Matsumoto, N., Kitagawa, Y., Takeda, N.,  
729 Kimura, H., Kimura, T., Matzuzawa, T., Shiomi, K., 2016. Short-term slow slip events  
730 in the Tokai area, the Kii Peninsula and the Shikoku District, Japan (from May 2015 to  
731 October 2015). Report of the Coordinating Committee for Earthquake Prediction 95.

732 Peng, Y., Rubin, A.M., 2016. High-resolution images of tremor migrations beneath the  
733 Olympic Peninsula from stacked array of arrays seismic data. *Geochem., Geophys.,  
734 Geosyst.* 17, 587–601. doi:10.1002/2015GC006141.

735 Peng, Y., Rubin, A.M., 2017. Intermittent tremor migrations beneath Guerrero, Mexico,  
736 and implications for fault healing within the slow slip zone. *Geophys. Res. Lett.* 44,  
737 2016GL071614. doi:10.1002/2016GL071614.

738 Peng, Y., Rubin, A.M., 2018. Simulating short-term evolution of slow slip influ-  
739 enced by fault heterogeneities and tides. *Geophys. Res. Lett.* 45, 10,269–10,278.  
740 doi:10.1029/2018GL078752.

741 Peng, Y., Rubin, A.M., Bostock, M.G., Armbruster, J.G., 2015. High-resolution imaging  
742 of rapid tremor migrations beneath southern Vancouver Island using cross-station cross  
743 correlations. *J. Geophys. Res.* 120, 4317–4332. doi:10.1002/2015JB011892.

744 Romanet, P., Bhat, H.S., Jolivet, R., Madariaga, R., 2018. Fast and slow slip events  
745 emerge due to fault geometrical complexity. *Geophys. Res. Lett.* 45, 4809–4819.  
746 doi:10.1029/2018GL077579.

747 Rousset, B., Campillo, M., Lasserre, C., Frank, W.B., Cotte, N., Walpersdorf, A., Socquet,

748 A., Kostoglodov, V., 2017. A geodetic matchedfilter search for slow slip with application  
749 to the Mexico subduction zone. *J. Geophys. Res.* doi:10.1002/2017JB014448.

750 Royer, A.A., Thomas, A.M., Bostock, M.G., 2015. Tidal modulation and triggering  
751 of low-frequency earthquakes in northern Cascadia. *J. Geophys. Res.* 120, 384–405.  
752 doi:10.1002/2014JB011430.

753 Rubin, A.M., 2008. Episodic slow slip events and rate-and-state friction. *J. Geophys. Res.*  
754 113, B11414. doi:10.1029/2008JB005642.

755 Rubin, A.M., 2011. Designer friction laws for bimodal slow slip propagation speeds.  
756 *Geochem., Geophys., Geosyst.* 12, Q04007. doi:10.1029/2010GC003386.

757 Rubin, A.M., Armbruster, J.G., 2013. Imaging slow slip fronts in Cascadia with high  
758 precision cross-station tremor locations. *Geochem., Geophys., Geosyst.* 14, 5371–5392.  
759 doi:10.1002/2013GC005031.

760 Savard, G., Bostock, M.G., 2015. Detection and location of lowfrequency earthquakes using  
761 crossstation correlation. *Bull. Seis. Soc. Amer.* 105, 2128–2142. doi:10.1785/0120140301.

762 Schmidt, D.A., Gao, H., 2010. Source parameters and time-dependent slip distributions of  
763 slow slip events on the Cascadia subduction zone from 1998 to 2008. *J. Geophys. Res.*  
764 115, B00A18. doi:10.1029/2008JB006045.

765 Segall, P., Rice, J.R., 1995. Dilatancy, compaction, and slip instability of a fluid-infiltrated  
766 fault. *J. Geophys. Res.* 100, 22155–22171. doi:10.1029/95JB02403.

767 Segall, P., Rubin, A.M., Bradley, A.M., Rice, J.R., 2010. Dilatant strengthening as a mech-  
768 anism for slow slip events. *J. Geophys. Res.* 115, B12305. doi:10.1029/2010JB007449.

769 Sekine, S., Hirose, H., Obara, K., 2010. Along-strike variations in short-term slow  
770 slip events in the southwest Japan subduction zone. *J. Geophys. Res.* 115, B00A27.  
771 doi:10.1029/2008JB006059.

772 Shelly, D.R., 2010. Migrating tremors illuminate complex deformation beneath the seismo-  
773 genic San Andreas fault. *Nature* 463, 648–652. doi:10.1038/nature08755.

774 Shelly, D.R., 2017. A 15year catalog of more than 1 million low-frequency earthquakes:  
775 Tracking tremor and slip along the deep San Andreas Fault. *J. Geophys. Res.* 122, 3739–  
776 3753. doi:10.1002/2017JB014047.

777 Shelly, D.R., Beroza, G.C., Ide, S., Nakamura, S., 2006. Low-frequency earthquakes in  
778 Shikoku, Japan, and their relationship to episodic tremor and slip. *Nature* 442, 188–191.  
779 doi:10.1038/nature04931.

780 Shibazaki, B., Iio, Y., 2003. On the physical mechanism of silent slip events along the deeper  
781 part of the seismogenic zone. *Geophys. Res. Lett.* 30, 1489. doi:10.1029/2003GL017047.

782 Shibazaki, B., Shimamoto, T., 2007. Modelling of short-interval silent slip events in deeper  
783 subduction interfaces considering the frictional properties at the unstable-stable transition  
784 regime. *Geophys. J. Intern.* 171, 191–205. doi:10.1111/j.1365-246X.2007.03434.x.

785 Skarbek, R.M., Rempel, A.W., Schmidt, D.A., 2012. Geologic heterogeneity can produce  
786 aseismic slip transients. *Geophys. Res. Lett.* 39, L21306. doi:10.1029/2012GL053762.

787 Sun, W.F., Peng, Z., Lin, C.H., Chao, K., 2015. Detecting deep tectonic tremor in Taiwan  
788 with a dense array. *Bull. Seis. Soc. Amer.* 105, 1349–1358. doi:10.1785/0120140258.

789 Supino, M., Poiata, N., Festa, G., Vilotte, J.P., Satriano, C., Obara, K., 2020. Self-similarity  
790 of low-frequency earthquakes. *Scientific Reports* 10, 6523. doi:10.1038/s41598-020-63584-  
791 6.

792 Takeo, A., Idehara, K., Iritani, R., Tonegawa, T., Nagaoka, Y., Nishida, K., Kawakatsu,  
793 H., Tanaka, S., Miyakawa, K., Iidaka, T., Obayashi, M., Tsuruoka, H., Shiomi, K.,  
794 Obara, K., 2010. Very broadband analysis of a swarm of very low frequency earth-  
795 quakes and tremors beneath Kii Peninsula, SW Japan. *Geophys. Res. Lett.* 37, L06311.  
796 doi:10.1029/2010GL042586.

797 Thomas, A.M., Beeler, N.M., Bletery, Q., Burgmann, R., Shelly, D.R., 2018. Using low-  
798 frequency earthquake families on the San Andreas Fault as deep creepmeters. *J. Geophys.*  
799 *Res.* 123, 457–475. doi:10.1002/2017JB014404.

800 Thomas, A.M., Beroza, G.C., Shelly, D.R., 2016. Constraints on the source parameters of  
801 low-frequency earthquakes on the San Andreas Fault. *Geophys. Res. Lett.* 43, 1464–1471.  
802 doi:10.1002/2015GL067173.

803 Thomas, T.W., Vidale, J.E., Houston, H., Creager, K.C., Sweet, J.R., Ghosh, A., 2013.  
804 Evidence for tidal triggering of high-amplitude rapid tremor reversals and tremor streaks  
805 in northern Cascadia. *Geophys. Res. Lett.* 40, 4254–4259. doi:10.1002/grl.50832.

806 Tu, Y., Heki, K., 2017. Decadal modulation of repeating slow slip event activity in the

807 southwestern Ryukyu Arc possibly driven by rifting episodes at the Okinawa Trough.  
808 Geophys. Res. Lett. 44, 9308–9313. doi:10.1002/2017GL074455.

809 UNAVCO, 2005. Plate Boundary Observatory, EarthScope. Dataset / seismic network.  
810 University of Washington, 1963. Pacific Northwest Seismic Network. Interna-  
811 tional Federation of Digital Seismograph Networks. Dataset / seismic network.  
812 doi:<https://doi.org/10.7914/SN/UW>.

813 Vaca, S., Valle, M., Nocquet, J.M., Battaglia, J., Rgnier, M., 2018. Recurrent slow slip events  
814 as a barrier to the northward rupture propagation of the 2016 Pedernales earthquake  
815 (Central Ecuador). *Tectonophysics* 724-725, 80–92. doi:10.1016/j.tecto.2017.12.012.

816 Walter, J.I., Schwartz, S.Y., Protti, M., Gonzalez, V., 2013. The synchronous occurrence  
817 of shallow tremor and very low frequency earthquakes offshore of the Nicoya Peninsula,  
818 Costa Rica. *Geophys. Res. Lett.* 40, 1517–1522. doi:10.1002/grl.50213.

819 Wang, J., Dennise C. Templeton, Harris, D.B., 2015. Discovering new events beyond the  
820 catalogue application of empirical matched field processing to Salton Sea geothermal field  
821 seismicity. *Geophys. J. Intern.* 203, 22–32. doi:10.1093/gji/ggv260.

822 Wech, A.G., Bartlow, N.M., 2014. Slip rate and tremor genesis in Cascadia. *Geophys. Res.*  
823 *Lett.* 41, 392–398. doi:10.1002/2013GL058607.

824 Wech, A.G., Creager, K.C., Melbourne, T.I., 2009. Seismic and geodetic constraints on  
825 Cascadia slow slip. *J. Geophys. Res.* 114, B10316. doi:10.1029/2008JB006090.

826 Wei, M., Kaneko, Y., Shi, P., Liu, Y., 2018. Numerical modeling of dynamically triggered  
827 shallow slow slip events in New Zealand by the 2016 Mw 7.8 Kaikoura earthquake. *Geo-*  
828 *phys. Res. Lett.* 45, 4764–4772. doi:10.1029/2018GL077879.

829 Yabe, S., Baba, S., Tonegawa, T., Nakano, M., Takemura, S., 2021. Seismic energy radiation  
830 and along-strike heterogeneities of shallow tectonic tremors at the Nankai Trough and  
831 Japan Trench. *Tectonophysics* 800, 228714. doi:10.1016/j.tecto.2020.228714.

832 Yamashita, Y., Yakiwara, H., Asano, Y., Shimizu, H., Uchida, K., Hirano, S., Umakoshi,  
833 K., Miyamachi, H., Nakamoto, M., Fukui, M., Kamizono, M., Kanehara, H., Yamada, T.,  
834 Shinohara, M., Obara, K., 2015. Migrating tremor off southern Kyushu as evidence for slow  
835 slip of a shallow subduction interface. *Science* 348, 676–679. doi:10.1126/science.aaa4242.

836 Zheng, G., Rice, J.R., 1998. Conditions under which velocity-weakening friction allows a  
837 self-healing versus a cracklike mode of rupture. *Bull. Seis. Soc. Amer.* 88, 1466–1483.